An analytical plane-strain solution for surface uplift due to pressurized reservoirs

Magnus Wangen

IFE, P.O.Box 40, N-2027 Kjeller, Norway

Gotskalk Halvorsen

IFE, P.O.Box 40, N-2027 Kjeller, Norway

Sarah E. Gasda

UNI Research CIPR, P.O.Box 7810, 5020 Bergen, Norway

Tore Bjørnarå

NGI, P.O.Box 3930, 0855 Oslo, Norway

Abstract

In this paper, we present an analytical plane strain solution for surface uplift above pressurized reservoirs. The solution is based on a Fourier representation of the reservoir pressure. The plane strain model is developed in two stages: First, an exact solution is derived for the displacement field for the reservoir alone subjected to a periodic overpressure distribution of one wavelength. This one-layer model forms the basis for the analytical plane strain solution for a two-layer model – a pressurized reservoir with an overburden. We give an example where numerically computed uplift is quite accurately estimated by a simple 1D estimate, except for in the near well area. The plane-strain solution is well suited to study conditions for when the simple 1D approximation of the uplift is accurate. A condition for the accuracy of the simple 1D approximation is first derived for just the reservoir expanded by a periodic overpressure distribution of one wavelength, which corresponds to one term in a Fourier series. The 1D estimate is accurate for wavelengths larger than 2π times the reservoir thickness. Then, a condition is derived for when the 1D estimate is accurate for the two-layer model. We show that the wavelength of the overpressure distribution must be larger than 2π times the maximum of the reservoir thickness and the overburden thickness for the 1D approximation to be accurate. We demonstrate how uplift is computed from a Fourier decomposition of the reservoir overpressure. The resulting uplift is analysed in terms of Fourier coefficients, using the knowledge of how a single wavelength behaves. The analytical results for the displacement field and the uplift are tested by comparison with finite element simulations, and the match is excellent.

Email address: Magnus.Wangen@ife.no (Magnus Wangen)

Keywords: Reservoir injection; geomechanics; surface uplift; poroelasticity

1. Introduction

The global emissions of CO_2 to the atmosphere are more than 35 Gt annually [17]. CO_2 is a greenhouse gas and the enormous emissions are one explanation for the observed global warming [10]. Subsurface storage of CO_2 in deep saline aquifers and depleted oil and gas reservoirs is considered a promising way to reduce the CO_2 emissions to the atmosphere [4, 5, 6]. The injection of large quantities of CO_2 into an aquifer or a reservoir leads to a build-up of pore fluid pressure. An increasing pore fluid will in turn lead to an expansion of the storage unit. Such expansion has been measured as surface uplift at the In Salah gas field using remote sensing techniques [27]. At In Salah, roughly 1 Mt CO_2 has been injected into a 20 m thick sandstone aquifer over 7 years [33]. The uplift is observed at a rate of roughly 5 mm/y around three injection wells [33]. A considerable amount of scientific interest has been devoted to understand surface uplift at In Salah and what it might imply for reservoir integrity [39, 35, 8, 40, 47, 33, 38, 29, 31, 46, 42, 30, 41]. In the same way as the onshore field In Salah, seabed uplift is expected for offshore CO_2 storage sites, although it is currently not straightforward to observe.

The surface uplift at In Salah has been modelled using numerical tools, like the mechanics simulator FLAC coupled to the two-phase flow simulator TOUGHREACT-II. The coupling of simulators for geomechanics and the multiphase flow is not a simple matter and the simulations are computer demanding [34, 28, 32, 1, 23].

However, it is possible to estimate the uplift from just the pressure response in the reservoir using an analytical 1D linear poroelastic model [11, 33]. Rutqvist [33] discuss the application of the 1D approximation at the In Salah site and he concludes that it overestimates the uplift near the wells. The overestimation is explained by the lateral variations of the fluid overpressure distribution in the reservoir, which are too large for a 1D model to be accurate. Such 1D estimates are very useful, since they can be applied directly to the pressure field from flow simulations, especially when the flow simulations can be performed decoupled from the geomechanics [9]. This method is extremely efficient when coupled with reduced order models for pressure increase from high volume injection of CO_2 into heterogeneous systems with large areal extent [13]. This simple method is therefore an attractive approach, however, its range of validity has been poorly quantified.

Analytical and semi-analytical models have been developed for the geomechanical response related to fluid injection into reservoirs and aquifers. Li et al. [24] present a semi-analytical model of a deformable reservoir coupled with immiscible two-phase flow (CO_2 and brine). The overburden is treated as a thin plate and the model computes axisymmetric flexural deformations due to a constant rate of CO_2 injection. The model is computationally light compared to the finite element simulations and it has been successfully applied to the In Salah field.

The full set of poroelastic equations can be computationally demanding to solve numerically. Therefore, it is customary to solve for the pore fluid pressure and the displacement field decoupled. One way to solve the poroelastic equations decoupled is by

means of the fixed-stress split, which assures that a sequential solution of the two equations is unconditionally stable [19, 20]. Another approach is developed by Andersen et al. [3, 2] by using precomputed response functions.

A problem related to uplift by fluid injection is subsidence caused by fluid production. An early example of a subsidence model, based on poroelasticity and cylinder coordinates, was developed by Geertsma [14, 15]. Selvadurai [36], Kim and Selvadurai [18], Selvadurai and Kim [37], Niu et al. [26] have developed analytical models for different configurations of a reservoir and a caprock. Selvadurai and Kim [37] present analytical poroelastic solutions for a storage aquifer with a caprock, when there is a steady injection into a circular injection zone. The analytical solutions are given as integral representations and they are rather complicated expressions. The solutions were used to investigate how the radius and the depth of the planar injection region influence the surface displacement.

It should be mentioned that analytical solutions have limited applicability with respect to complicated geometries and complicated distributions of material properties. As with the analytical models cited in the paragraph above, we assume long sedimentary strata of homogeneous rocks. The challenge of upscaling heterogeneous rock units is outside the scope of this article.

In this paper, we develop a plane-strain solution of the displacement field for an overpressured reservoir with an overburden. We do this in terms of stationary analytical solutions of the poroelastic equations, when the reservoir overpressure is represented by a Fourier series. The reservoir layer is of infinite lateral extent with a periodic overpressure distribution. Overpressure is defined as the fluid pressure minus the initial fluid pressure, where the initial pressure is assumed hydrostatic. The expression for the displacement field gives the surface uplift. The solution is developed in two steps: The first is a one-layer model of just an overpressured reservoir. The next step, which builds on the first step, is a two-layer model of an overpressured reservoir with an overburden. These solutions for the displacement field are first developed for pressure as a single cosine-function, which is one term in a Fourier series. The one-layer and two-layer models are well suited to study the accuracy of a 1D estimate of uplift from a reservoir overpressure. We give answers in terms of wavelength. The poroelastic mechanical model is linear. Therefore, the full solution of the displacement field and the uplift is found as a superposition of solutions for the terms in the Fourier series representing the reservoir pressure. The use of plain strain assumption and Cartesian coordinates is different from the other approaches mentioned above, which are based on cylindrical coordinates. Another difference is that we study how a stationary fluid pressure controls the mechanical deformations, with respect to wavelengths.

This paper is organized as follows: The poroelastic assumptions are reviewed and an example is given where numerical computed uplift is compared with the 1D poroelastic uplift. The analytical model for the expansion of the reservoir is presented, before the analytical model for a reservoir layer with an overburden. The analytical results for uplift are first tested against numerical simulations for a single wavelength and then for pressure distributions represented by Fourier series.

2. Poroelasticity

The initial stress state is not modelled – it is taken as given. The difference from the initial stress state is modelled assuming linear poroelasticity [7, 43]. Therefore, the full stress state is written as

$$\sigma_{ij} = \sigma_{ij}^{(0)} + \sigma_{ij}^{(1)} \tag{1}$$

where $\sigma_{ij}^{(0)}$ is the initial stress and where $\sigma_{ij}^{(1)}$ is the poroelastic stress change caused by fluid injection. The full stress state fulfills the equilibrium equations

$$\sigma_{ij,j} = \varrho g \delta_{iz} \tag{2}$$

where g is the constant of gravity, ϱ is the bulk rock density and δ_{ij} is the Kronecker delta

$$\delta_{ij} = \begin{cases} 0, & i \neq j \\ 1, & i = j \end{cases} \tag{3}$$

The Einstein summation convention is applied in equilibrium equation (2), which means that there is summation over every pair of equal indices. The indices can have three values, 1, 2 and 3, which represent the three different spatial directions, respectively. An alternative to 1, 2 and 3 is x, y and z, respectively, with the exception that there are no summation over the x, y and z when they are used as indices. The initial stress state does also fulfill the equilibrium equations, which implies that the equilibrium equations in terms of the poroelastic stress difference becomes

$$\sigma_{ij,j}^{(1)} = 0 \tag{4}$$

where the right-hand-side is just zero. The right-hand-side of the equilibrium balance (4) could include a term representing buoyancy of supercritical CO_2 being less dense than brine. The following analysis is single phase and the eventual uplift from buoyancy is not accounted for, as commonly done with analytical models [15, 36, 37]. The effective stress τ_{ij} can be written as the sum of the initial effective stress $\tau_{ij}^{(0)}$ and the effective stress caused by changes in the fluid pressure $\tau_{ij}^{(1)}$, in a similar way to the full stress state

$$\tau_{ij} = \tau_{ij}^{(0)} + \tau_{ij}^{(1)} \tag{5}$$

The initial effective stress is the full stress added to the initial fluid pressure

$$\tau_{ij}^{(0)} = \sigma_{ij}^{(0)} + \alpha p^{(0)} \delta_{ij} \tag{6}$$

where $p^{(0)}$ is the initial fluid pressure and α is the Biot coefficient. The sign convention is that tension is positive strain and positive stress, while the fluid pressure is positive. The effective stress caused by fluid injection is written in the same way as

$$\tau_{ij}^{(1)} = \sigma_{ij}^{(1)} + \alpha p^{(1)} \delta_{ij} \tag{7}$$

where $p^{(1)}$ is the pressure that develops from fluid injection. It is the effective stress (7) that leads to linear poroelastic deformations

$$\sigma_{ij}^{(1)} + \alpha p^{(1)} \delta_{ij} = \Lambda \epsilon_{kk} \delta_{ij} + 2G\epsilon_{ij} \tag{8}$$

where $\epsilon = \frac{1}{2}(u_{i,j}+u_{j,i})$ is the strain, u_i is the deformation in spatial direction i, Λ is the Lameé-parameter and G is the shear modulus. The equations for the displacement field are obtained by inserting the stress $\sigma_{ij}^{(1)}$ into equilibrium equations (4). We assume zero strain in the y-direction, $\epsilon_{yy} = 0$, which leads to the following 2-dimensional model for the displacement field

$$(\Lambda + 2G)u_{,xx} + (\Lambda + G)w_{,xz} + Gu_{,zz} = \alpha p_{,x} \quad (9)$$

$$(\Lambda + 2G)w_{,zz} + (\Lambda + G)u_{,xz} + Gw_{,xx} = \alpha p_{,z} \quad (10)$$

where the notation is simplified using $u = u_1$ (without an index), $w = u_3$ and $p = p^{(1)}$. Equations (9)-(10) show how the displacement field is coupled to the fluid pressure.

Equations (9) and (10) give how the fluid pressure produces deformation in the rock. These deformations have a feedback on the fluid pressure through the change of volume strain. The equation for the fluid pressure is

$$\left(\frac{\phi}{K_f} + \frac{\alpha - \phi}{K_s}\right)\frac{\partial p}{\partial t} - \nabla\left(\frac{\kappa}{\mu}\nabla p\right) = -\alpha\frac{\partial \epsilon}{\partial t} \quad (11)$$

where K_s and K_f are the bulk modulus of the solid and the fluid, respectively, ϕ is the porosity, κ is the permeability, μ is the fluid viscosity and $\epsilon = \epsilon_{xx} + \epsilon_{yy} + \epsilon_{zz}$ is the bulk strain. The pressure is coupled to the displacement field through the source term $\partial\epsilon/\partial t$.

3. 1D vertical uplift

A simple and useful solution of the equations for the displacement field is the 1D vertical expansion of a reservoir layer under a constant pressure p_0. The pressure increase p_0 is restricted to the reservoir layer and there is no lateral displacement, $u = 0$. Then, equation (10) simples to $(\Lambda + 2G)w_{,zz} = \alpha p_{,z}$, which after two times of integration gives

$$w = \frac{\alpha p_0 (z - z_0)}{\Lambda + 2G}, \quad (12)$$

when there is zero vertical displacement at the base of the layer at $z = z_0$. The denominator $\Lambda + 2G$ is termed uniaxial modulus or the p-wave modulus. The maximum displacement at maximum the top of the layer becomes

$$w = \frac{\alpha p_0 h}{\Lambda + 2G} \quad (13)$$

where h is the layer thickness. This 1D model for reservoir expansion turns out to be a simple and accurate way to estimate surface uplift in certain situations of large scale fluid storage. Furthermore, when the approximation (13) is valid the time-derivative of the bulk strain becomes

$$\frac{\partial \epsilon}{\partial t} \approx \frac{\partial}{\partial t}\frac{\partial w}{\partial z} = \frac{\alpha}{(\Lambda + 2G)}\frac{\partial p}{\partial t} \quad (14)$$

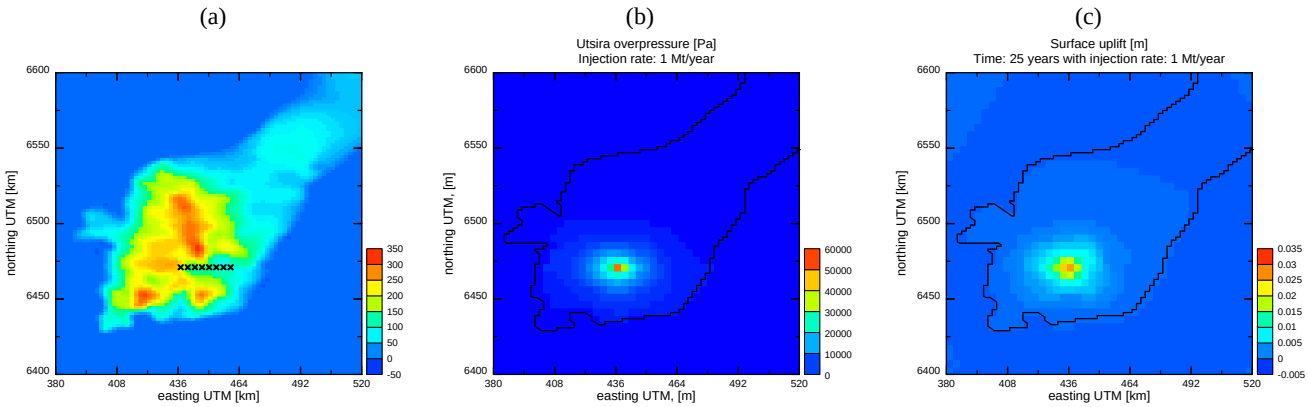

Figure 1: *(a) The figure shows the thickness of the Utsira formation, where the x'es mark the places where the uplift is logged. The x-mark to the left is the position of the injection well. (b) The overpressure in the Utsira formation after 25 years of injection. (c) The uplift of the seabed after 25 years of injection.*

When this is the case, it is possible to use relation (14) to decouple the pressure equation from the displacement field, since the pressure equation can be written [9, 25]

$$\left(\frac{\phi}{K_f}+\frac{\alpha-\phi}{K_s}+\frac{\alpha^2}{(\Lambda+2G)}\right)\frac{\partial p}{\partial t}-\nabla\left(\frac{k}{\mu}\nabla p\right)=0 \tag{15}$$

The advantages of this decoupling, when it is applied to model large scale poroelastic deformations from CO_2 injection, have been demonstrated by Bjørnarå et al. [9], Gasda et al. [13].

4. Numerically computed uplift compared with 1D uplift

This section gives an example of numerically computed surface uplift, which is compared with the estimate (13). The example is a case study of fluid injection into the Utsira formation in the Sleipner field in the North Sea. The Utsira formation is a more than 400 km long sandy aquifer of Pliocene age with a thickness in the range from 50 m to 350 m, see figure 1a. It is covered by a 500 m thick layer of fine grained Quaternary clay and shale, and by 100 m to 200 m seawater [44, 16]. The geomechanical model of the formation includes the caprock (the Nordland shale) the Utsira sand and the underburden, which is shale of Tertiary age. Geomechanical and petrophysical data for these units are limited and they are therefore treated as homogeneous rocks. The details of the model are found in Wangen et al. [44].

Figure 1a shows the isopach of the Utsira formation, which together with the fluid pressure (figure 1b) can be used to estimate the aquifer expansion and the surface uplift. Figure 1c shows the numerically computed uplift after 25 years of fluid injection. The lateral extent of the surface uplift is large compared to the thickness of the aquifer and

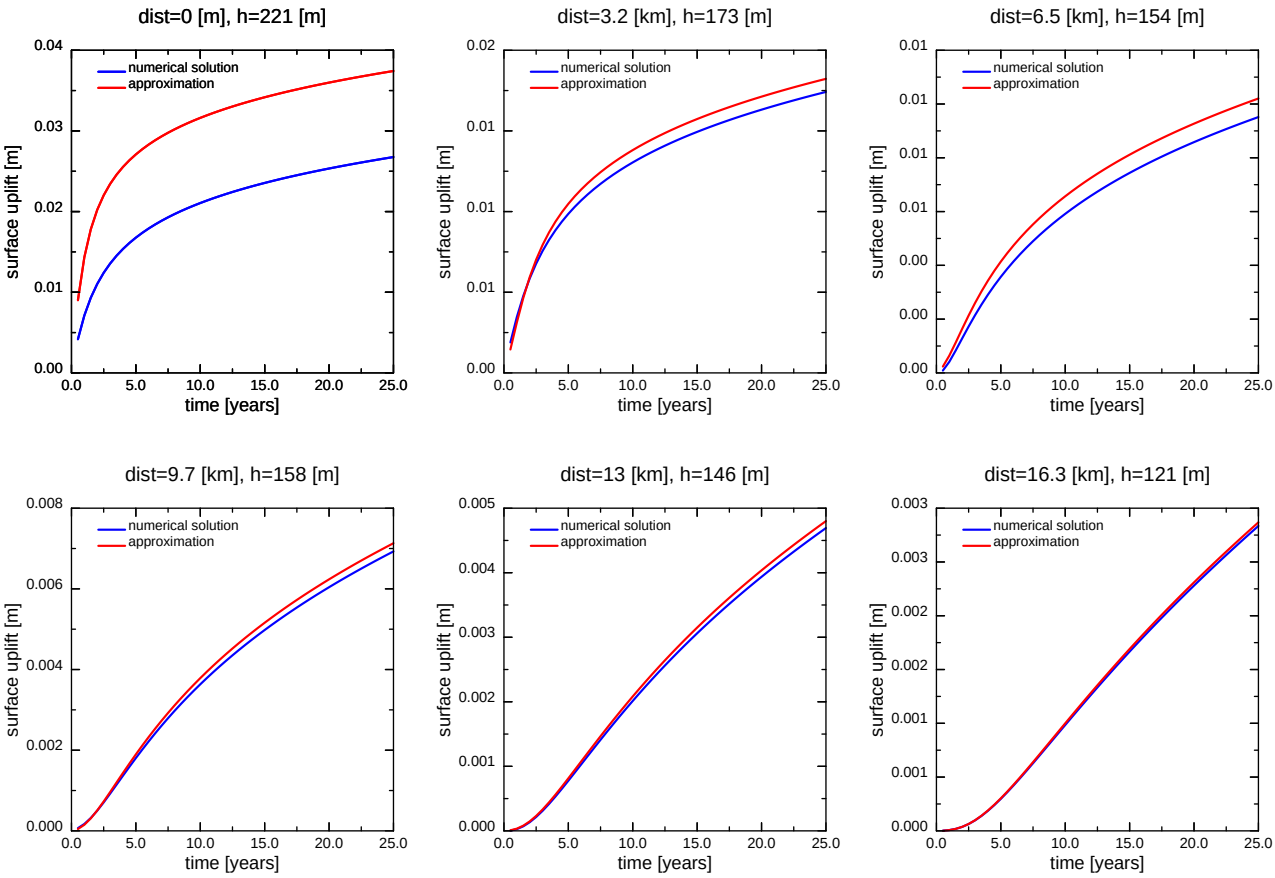

Figure 2: *The blue curve is the numerically computed uplift and the red curve is the uplift estimated with equation (13). The reservoir thickness and the distance from the injection well is denoted on the plots as "dist" and "h", respectively.*

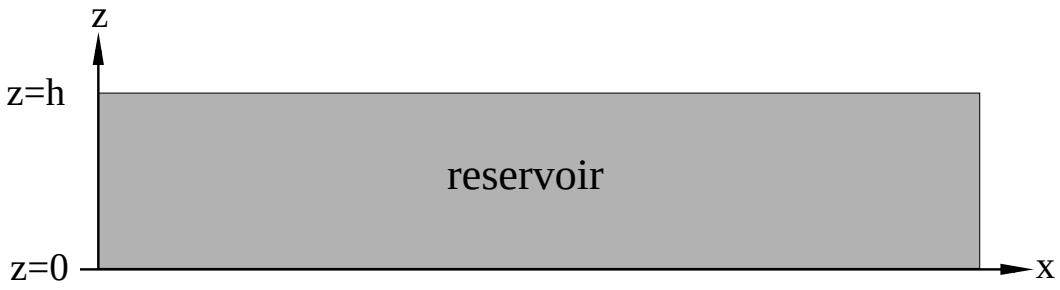

Figure 3: *The analytical model of the reservoir uplift is based on a reservoir of thickness h.*

the overburden. The surface uplift was logged as a function of time at the 6 position marked with an "x" on figure 1a. The leftmost mark shows the lateral position of the injection well.

The numerically computed uplift is compared with the estimated uplift using relationship (13) in figure 2. The uplift is compared over a time span of 25 years, where p_0 is equation (13) is the overpressure at the given time and place. Therefore, the pressure p_0 is a function of time in the uplift estimate (13). The estimated uplift is close to the uplift computed from the 3D poroelastic model. The difference is less than 30% above the injection element where the lateral change in fluid pressure is largest. There is a good match away from the injection element, which suggests that the estimate (13) might be useful as a simple way to estimate geomechanical deformations for certain injection scenarios. It is also seen from figure 2 how the uplift starts at increasingly later times with an increasing distance to the injection point. We will see that the reason for the better match away from the injection element is that the reservoir pressure is decreasing slowly with distance, which corresponds to a pressure distribution with long wavelengths in a Fourier decomposition.

5. Poroelastic expansion of a reservoir layer

The aim of this work is to find conditions that must be fulfilled for 1D vertical uplift to be a "good" approximation. The first step is to study the expansion and uplift of the reservoir layer alone, when the layer has a known overpressure distribution. Taking the pressure as known allows us to study how a given pressure distribution creates mechanical deformations. Since the pressure distribution is known, we are not solving the fully coupled poroelastic model. Figure 3 shows the reservoir layer with thickness h. The layer has lateral extent from $-L$ to L. We assume that the pressure distribution $p(x)$ inside the layer is symmetric around the z-axis ($x = 0$) and that it goes to zero before the domain size $x = L$. The pressure distribution is taken to be an even and periodic function and it can, therefore, be represented as follows by a Fourier series of cosine-functions,

$$p(x) = \frac{a_0}{2} + \sum_{n=1}^{\infty} a_n \cos(n\pi x/L) \tag{16}$$

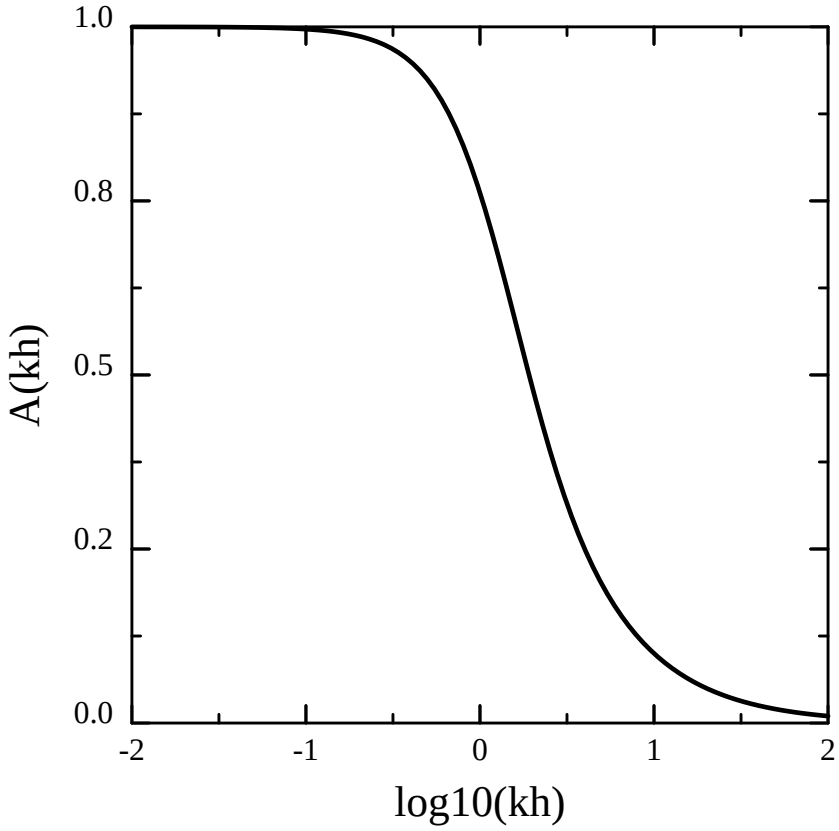

Figure 4: *The dimensionless amplitude (27) as a function of* $kh = 2\pi h/\lambda$.

where the Fourier coefficients a_n are given by

$$a_n = \frac{2}{L}\int_0^L p(x)\cos(n\pi x/L)\,dx, \qquad n = 0, 1, 2, \ldots \tag{17}$$

see for instance Kreyszig [21]. The Fourier series is periodic with period $2L$, because we have that $p(x + 2L) = p(x)$. The inaccuracy introduced by the assumption of a periodic pressure distribution approaches zero with increasing L [45]. There is no upper limit for the domain size in the analysis of uplift that we carry out below, although there is a lower limit, as we will see. It should also be mentioned that a Fourier analysis in the limit $L \to \infty$ gives the Fourier transform, which is not restricted to periodic functions [45]. Since the mechanical model is linear with respect to the fluid pressure, we can make a superposition of the contributions from the terms in the Fourier series. A particular aim with the model is to see how the uplift depends on the wavelength. We will therefore look at how a single term in the Fourier series affects the uplift. Therefore, we assume that the overpressure in the layer is a cosine-function

$$p(x) = p_0\cos(kx) \qquad \text{and} \qquad k = \frac{2\pi}{\lambda} \tag{18}$$

where p_0 is the maximum pressure, k is the wavenumber and λ is the wavelength. Since the cosine-function has a given wavelength and it is reasonable to expect that there will be a change in behaviour of the uplift as wavelength goes from "short" to "long". The model is expected to expand vertically for "long" wavelengths. The negative and the positive parts of the overpressure are expected to cancel for "short" wavelengths and the net effect is zero expansion.

The cosine representation of the overpressure can be inserted into the equations (9) and (10) for the displacement field, which gives that

$$(2+\gamma)u_{,xx} + u_{,zz} + (1+\gamma)w_{,xz} = -\frac{\alpha k p_0}{G}\sin(kx) \tag{19}$$

$$(1+\gamma)u_{,xz} + w_{,xx} + (2+\gamma)w_{,zz} = 0 \tag{20}$$

where $\gamma = \Lambda/G$ is a dimensionless elastic parameter. We notice that the Biot coefficient appears at only one place, as a factor together with the amplitude p_0 of the pressure. The boundary conditions for the pressurized aquifer is zero vertical displacement at its base

$$w(z{=}0) = 0 \tag{21}$$

and zero normal stress at the top, $z = h$,

$$\sigma_{zz}(z{=}h) = \Lambda\frac{\partial u}{\partial x} + (\Lambda + 2G)\frac{\partial w}{\partial z} - \alpha p_0\cos(kx) = 0 \tag{22}$$

The full stress is the effective stress minus the fluid pressure times the Biot coefficient, as given by the definition of effective stress (7). The solution (u, v) of the equations (19) and (20) for the displacement field becomes

$$u = \frac{\alpha p_0}{(2+\gamma)Gk}\left(1 - \frac{\cosh(kz)}{\cosh(kh)}\right)\sin(kx) \tag{23}$$

$$w = \frac{\alpha p_0}{(2+\gamma)Gk}\frac{\sinh(kz)\cos(kx)}{\cosh(kh)} \tag{24}$$

as shown in Appendix A. The displacement field is also periodic with the same wavelength λ as the reservoir pressure. The displacement in the x-direction is zero along the top surface and it is a sinus-function along the base surface with amplitude $\alpha p_0/((2+\gamma)Gk)$. The vertical displacement is a cosine-function with an amplitude that is proportional to the internal pressure (18). The amplitude has its maximum at the surface and it is zero at the base as imposed by the boundary condition. In order to see how the uplift depends on the wavelength it is instructive to write the displacement field in the following dimensionless form

$$\hat{u} = \frac{1}{kh}\left(1 - \frac{\cosh(kh\hat{z})}{\cosh(kh)}\right)\sin(2\pi\hat{x}) \tag{25}$$

$$\hat{w} = \frac{\sinh(kh\hat{z})}{kh\cosh(kh)}\cos(2\pi\hat{x}) \tag{26}$$

where $\hat{x} = x/\lambda$ $\hat{z} = z/h$, $\hat{u} = u/u_0$ and $\hat{w} = w/u_0$ where where $u_0 = \alpha p_0 h/(\Lambda + 2G)$. The characteristic displacement u_0 is precisely the 1D vertical uplift. Therefore, how the vertical uplift depends on the wavelength is represented by the dimensionless amplitude at the surface ($z = h$)

$$A(kh) = \frac{\tanh(kh)}{kh}. \tag{27}$$

The amplitude (27) is only a function of the dimensionless argument $kh = 2\pi h/\lambda$. It is plotted in figure 4, which shows that there is a transition from $A \approx 1$ for $kh \ll 1$ to $A \approx 0$ for $kh \gg 1$. Therefore, the 1D vertical uplift (13) is a good approximation for wavelengths sufficiently long to fulfill $kh \ll 1$, or alternatively, $\lambda \gg 2\pi h$. The pressure variations cancel out for short wavelengths, $\lambda \ll 2\pi h$. The critical wavelength $\lambda_c = 2\pi h$ defines the transition between the two regimes. We notice that condition for the use of approximation (13) does not depend on the poroelastic parameters G, ν and α – the condition is only dependent on the thickness of the aquifer.

6. Poroelastic uplift above a reservoir layer with an overburden

Aquifers being candidates for CO_2 storage are normally found at a depth of 1000 m or deeper, because that is the depth necessary for CO_2 to remain supercritical. Therefore, the overburden cannot be ignored when considering the uplift above aquifers and reservoirs for CO_2 storage.

A model with a reservoir and an overburden is shown in figure 5. The reservoir has the thickness h_1 and the overburden has the thickness h_2 and both are infinite in the x-direction, where the reservoir has the periodic overpressure distribution (18). The solutions for the displacement field (u_A, w_A) for the reservoir and (u_B, w_B) for the overburden are derived in Appendix B. These displacement fields are continuous on the interface between the reservoir and the overburden. The vertical displacement w_A is zero at the base of the reservoir and there is zero normal stress at the surface of the overburden.

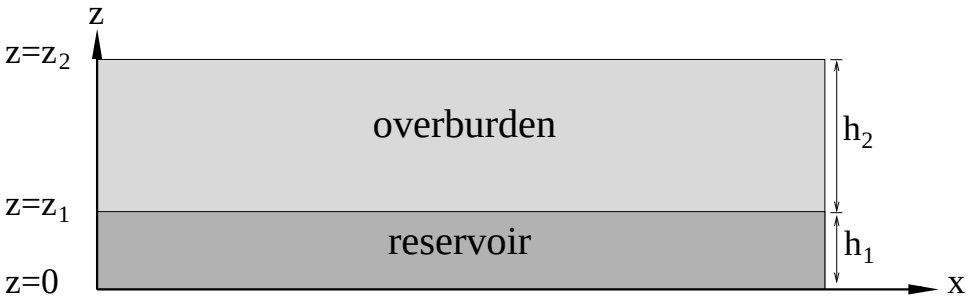

Figure 5: *The analytical model of the reservoir uplift is based on a rectangular reservoir under a rectangular caprock. The thickness of the reservoir is h_1 and the thickness of the caprock is h_2.*

The uplift is given by the displacement at the surface of the overburden, $w_B(z{=}z_2)$. From Appendix B, we have that

$$w_B(z{=}z_2) = \frac{\alpha p_0 h_1}{(\Lambda + 2G)} \cdot f(kh_1, kh_2) \cdot \cos(kx) \tag{28}$$

where the first factor is identified as the 1D vertical uplift. The second factor, the function f, is the dimensionless amplitude that depends on the layer thicknesses. It is given as

$$f(kh_1, kh_2) = \frac{1}{kh_1}\Big(\cosh(kh_2)\tanh(kh_1 + kh_2) - \sinh(kh_2)\Big) \tag{29}$$

as derived in Appendix B. The function (29) gives the same dimensionless amplitude as (27), for just the reservoir layer, when $h_2 = 0$. How the function (29) depends on both kh_1 and kh_2 is shown in the plot 6. We see that the function f is between 0 and 1, and that the regime where it is close to one is given by $kh_1 \ll 1$ and $kh_2 \ll 1$. This is the regime where the 1D vertical solution (13) is a good approximation. The other regimes, where either $kh_1 \gg 1$ or $kh_2 \gg 1$, have too short wavelength and the oscillations in the periodic fluid pressure (18) cancel out. There is a transition zone between the regimes of $f \approx 1$ and $f \approx 0$, which takes place in either of the two cases: (1) $hk_1 \approx 1$ and $hk_2 \ll 1$, (2) $hk_1 \ll 1$ and $hk_2 \approx 1$. In terms of the wavelength of the periodic pressure the condition for the validity of the 1D approximation can be written as

$$\lambda \gg \lambda_c \qquad \text{and} \qquad \lambda_c = 2\pi \max(h_1, h_2), \tag{30}$$

where the lower limit on wavelength is λ_c.

In order to represent the long wavelengths that allows for the 1D solution of uplift, we need a minimum domain size L. The wavelengths in the Fourier series (16) are $\lambda_n = 2L/n$ for $n = 1, 2, \ldots$. According to condition (30), we must therefore have $\lambda_n > \lambda_c$ for $n = 1, 2, \ldots, n_0$, where n_0 is a suitable number of long wavelengths. A slightly stronger condition is $\lambda_n > 2\pi H$, where $H = h_1 + h_2$. An alternative is to write this condition as $L > \pi n_0 H$ or simply $L \gg 2\pi H$. We also notice that the

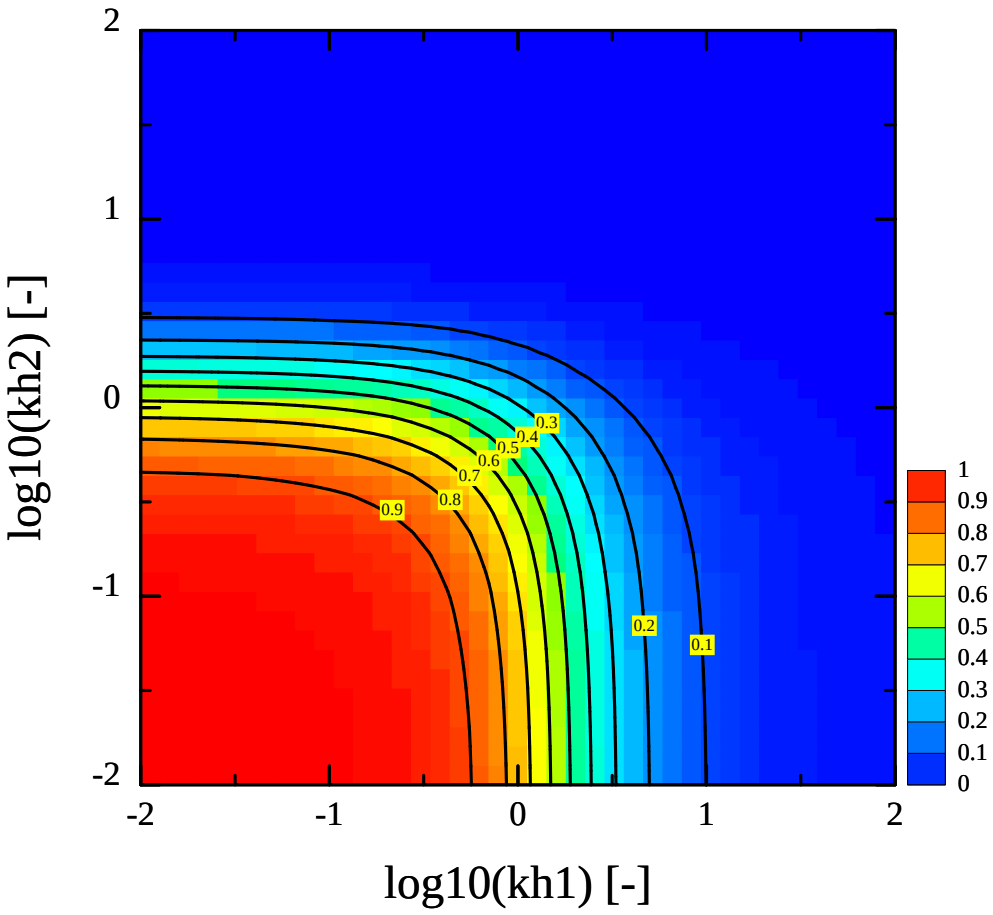

Figure 6: *The dimensionless amplitude (29) plotted as a function of* $\log_{10}(kh_1)$ *and* $\log_{10}(kh_2)$.

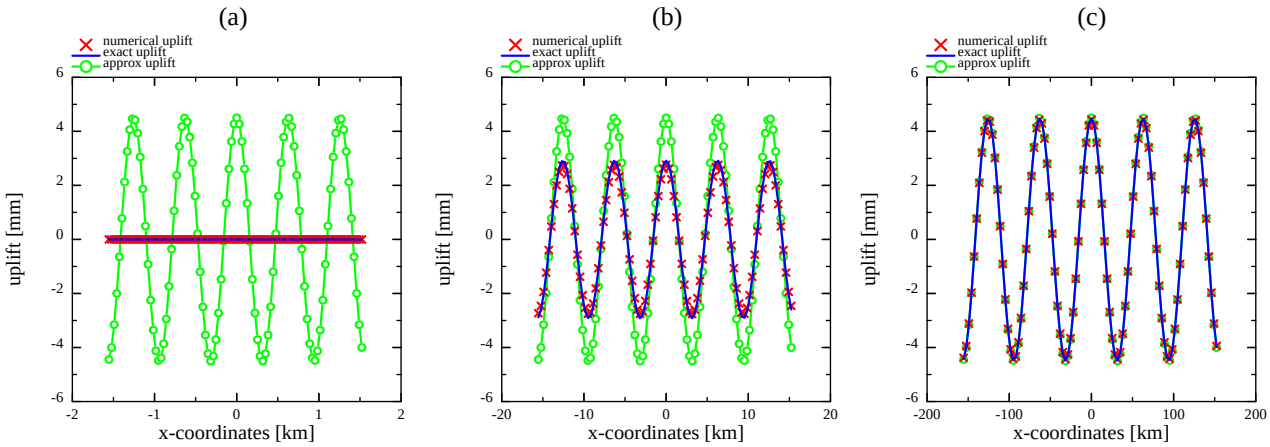

Figure 7: *A numerical check of the analytical solution (28) in the three different regimes of wavelength: (a)* $\lambda/\lambda_c = 0.1$*, (b)* $\lambda/\lambda_c = 1$*, (c)* $\lambda/\lambda_c = 10$*, where* $\lambda_c = 2\pi h_2$ *with* $h_2 = 1000$ *m. The reservoir layer has the thickness* $h_1 = 50$ *m and the pressure amplitude is* $p_0 = 1$ *MPa.*

amplitude a_0 in the series (16), which corresponds to an infinite long wavelength, goes to zero with an increasing domain size and an increasing number of long wavelengths.

7. Numerical verification

The analytical result (28) for uplift was tested by comparing them with numerical simulations. The uplift given by equation (28) is for just one term in a Fourier series for overpressure and it is not an injection pressure. The numerical code solves the displacement equations with a standard finite element method [22]. Bilinear rectangular elements for the mechanics problem is used in combination with the pressure represented at the element centers. The code assumes plain strain in the xz-plane and the periodic overpressure distribution (18). The thickness of the reservoir layer is $h_1 = 50$ m and the thickness of the overburden is $h_2 = 1000$. Both the reservoir and the overburden have the same Lameé-parameter $\Lambda = 2.778$ GPa, shear modulus $G = 4.167$ GPa and Biot coefficient $\alpha = 1$. (The elastic parameters are equivalent to Young's modulus $E = 10$ GPa and Poisson ratio $\nu = 0.2$.) The pressure amplitude is $a_0 = 1$ MPa and it is seen that displacement field is proportional to p_0. From equation (13) and the numbers above we get that the 1D uplift, resulting from the expansion of the reservoir, is $w = 4.5$ mm. The finite element grid has $100 \times 15 = 1500$ nodes. The lower boundary on the wavelength for the 1D approximation (13) is $\lambda_c = 2\pi h_2 = 6283.2$ m. Figure 7 shows three cases with wavelengths $\lambda = 0.1\lambda_c$, $\lambda = \lambda_c$ and $\lambda = 10\lambda_c$ in figures (a), (b) and (c), respectively. All cases show uplift for 5 periods of the overpressure distribution. The match between the numerical finite element solutions (red crosses) and the corresponding analytical solutions (blue curve) is good.

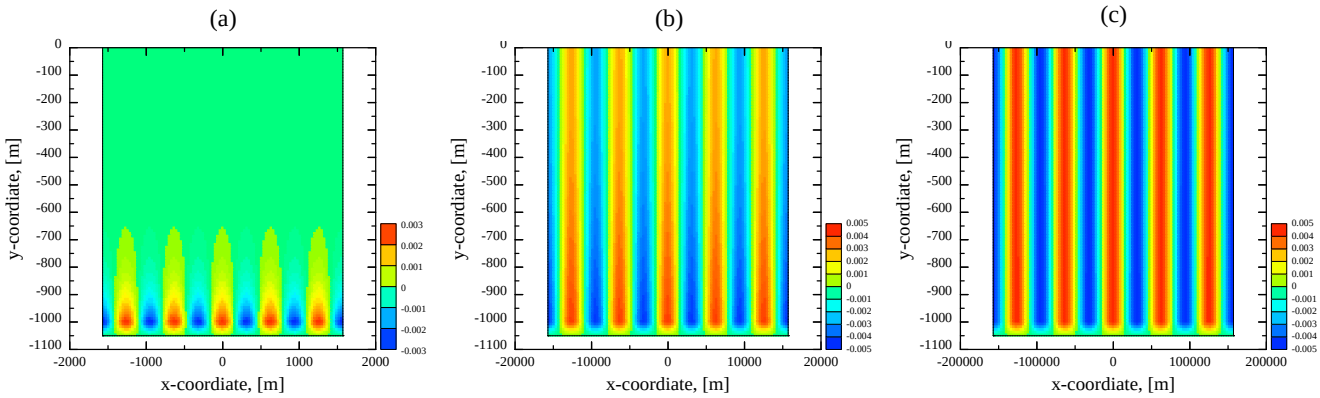

Figure 8: *The analytical vertical displacement field, w_A (for $z < h_1$) and w_B (for $z > h_1$), is shown for three different regimes of wavelength: (a) $\lambda/\lambda_c = 0.1$, (b) $\lambda/\lambda_c = 1$, (c) $\lambda/\lambda_c = 10$, where $\lambda_c = 2\pi h_2$ with $h_2 = 1000$ m. The reservoir layer has the thickness $h_1 = 50$ m and the pressure amplitude is $p_0 = 1$ MPa.*

Figure 7 shows that the vertical deformation are more than half-way towards its maximum value when $\lambda = \lambda_c$. Therefore, the approximation may be useful even for wavelengths down to λ_c. The numerical example presented in the section 4 has a finite element grid with xy-resolution $dx = 3265$ m and $dy = 4900$ m. The thickness of the overburden is a little less than 1000 m, and the limiting wavelength becomes $\lambda_c \approx 6000$ m. The limit λ_c is short compared with the cell size dx and dy, since only few cells are enough to cover the size λ_c. This is consistent with the good match away from the injection point, shown in figure 1, between the numerically computed uplift and the estimated uplift. It should be mentioned that the analytical results give a condition assuming plain-strain, while the case in figure 1 is not plain-strain.

Figure 8 shows the full vertical displacement field, which is w_A for $z \leq h_1$ and w_B for $z > h_1$. The surface uplift in figure 7 is the displacement at the surface ($z = 0$) model in figure 8. Figure 8 shows that the vertical displacement is zero at the base $z = -1050$ m and it increases towards the top of the reservoir at $z = -1000$ m, where it is at its maximum. For short wavelengths, $\lambda \ll \lambda_c$, the vertical displacement is decreasing in the overburden towards the surface. It is almost zero in the upper part of the overburden, and there is no surface uplift. For the critical wavelength, $\lambda = \lambda_c$, the vertical displacements are only partly suppressed by the overburden, and there is noticeable surface uplift as seen from the figure 7b. In the case of long wavelength, $\lambda = 10\lambda_c$, the maximum vertical displacement at the top of the reservoir is preserved through the entire caprock, and the surface uplift is almost the same as the expansion of the reservoir.

Even if it is not rigorously proved, experience with the plain-strain results indicate that the condition (30) is useful for assessing the uplift in a general setting in 3D with a variable layer thickness. The 1D estimate (13) is accurate when the wavelength in

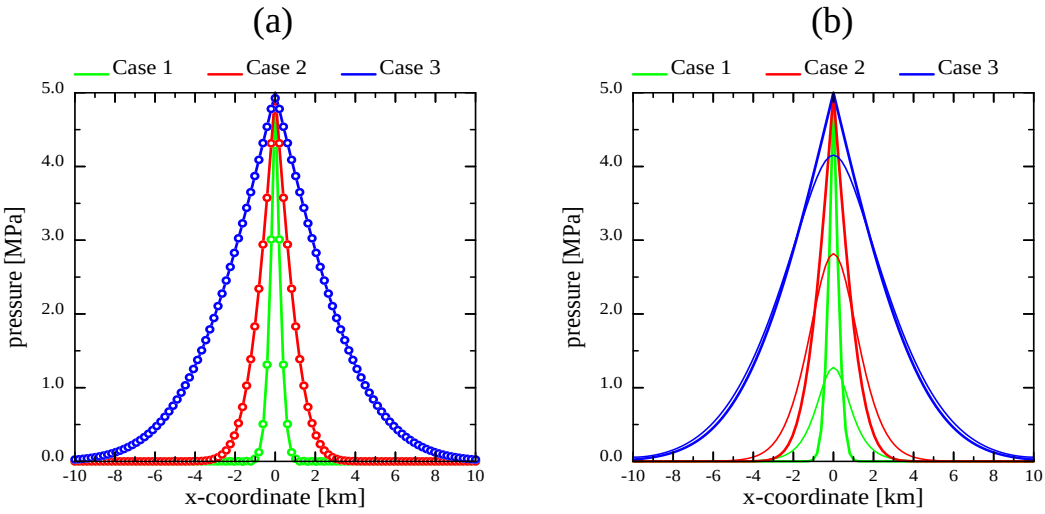

Figure 9: *The thick line shows the three pressure distributions of the cases 1, 2 and 3, which corresponds to* 0.1, 1 *and* 10 *years of injection, respectively. (a) The circular markers show the Fourier representation of the pressure distributions. (b) The thin line show the pressure* $p_u(x)$ *of equation (32). See the text for further explanation.*

both the x- and y-directions of the overpressure distribution is much larger than λ_c, and when λ_c is based on maximum layer thicknesses.

8. Computation of uplift from Fourier representations of reservoir overpressure

The previous section looks at the uplift from the pressure represented by just a single wavelength, which could be one term in a Fourier series. Now, we will give examples of uplift from more realistic pressure distributions, which are represented by Fourier series. We consider the pressure distributions obtained by injecting fluid at a constant overpressure $p_0 = 5$ MPa at $x = 0$. The overpressure is then given by the following solution of the pressure equation (11)

$$p(x,t) = p_0 \operatorname{erfc}\Big(\frac{x}{2\sqrt{Dt}}\Big) \tag{31}$$

where $D = \kappa K_f/(\mu\phi)$ is the hydraulic diffusivity. The hydraulic diffusivity is $D = 0.02$ m^{2}s^{-1}, which is the result of the following set of parameters: $\kappa = 1 \cdot 10^{-13}$ m^2, $\phi = 0.1$, $\mu = 0.001$ Pa s and $K_f = 2 \cdot 10^7$ Pa. The rock parameters are Young's modulus $E = 10$ GPa, Poisson ratio $\nu = 0.2$ and Biot coefficient $\alpha = 1$. Since $E \gg K_f$, fluid compressibility dominates the rock compressibility and the right hand side of equation (11) can be ignored.

Three pressure distributions are produced with solution (31), selecting the times $t = 0.1$ year, 1 year and 10 years, see figure 9. They are termed case 1, 2 and 3,

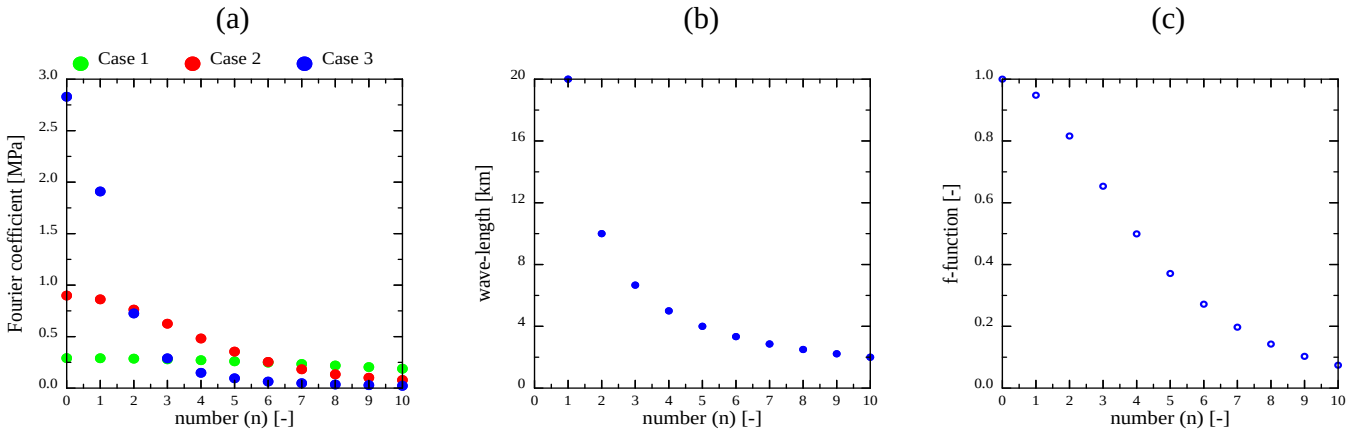

Figure 10: *(a) The 11 first Fourier coefficients in the pressure distributions shown in figure 9. (b) The 11 first wavelengths. (c) The f-function (29) for the same numbers as in figure (a) and (b). Notice that the three different pressure distributions in figure 9 have the same wavelengths and therefore the same f-function values.*

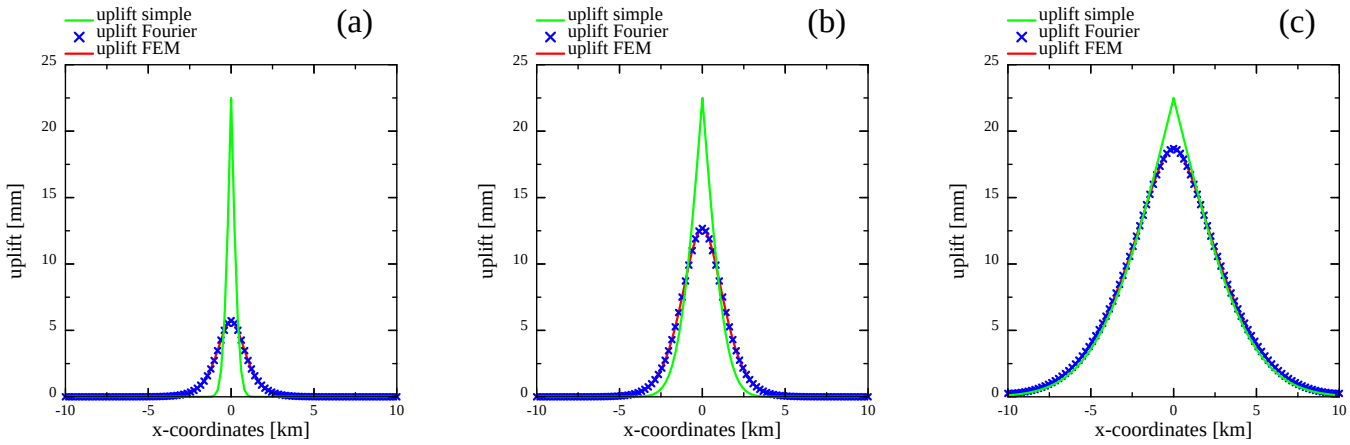

Figure 11: *The uplift created by the three pressure distributions in figure 9.*

respectively. The pressure distributions are represented by the Fourier series (16), and the Fourier representation is plotted in figure 9a with circular markers. The Fourier series are seen to provide an accurate representation of the given fluid pressure. The 11 first Fourier coefficients a_n of the series are plotted in figure 10, and they are computed by numerical integration of integral (17). It should be noted that the procedure to represent a pressure distribution by the Fourier series (16) is general and not restricted to solution (31). The solution (31) just serves as the basis for an example.

The uplift from one term in the Fourier series is given by equation (28). Since equations (9) and (10) for the displacement field are linear we can superpose the contributions from each term in the Fourier series for pressure. Therefore, the uplift from the series (16) becomes

$$w(x) = \frac{\alpha h_1 p_u(x)}{(\Lambda + 2G)} \quad \text{where} \quad p_u(x) = \frac{a_0}{2} + \sum_{n=1}^{\infty} f(k_n h_1,\, k_n h_2)\, a_n \cos(k_n x). \quad (32)$$

The uplift produced by the three discrete pressure distributions in figure 9 are shown in figure 11. Figure 11 shows three curves for each case, where the first is red and it shows the uplift computed by a finite element simulation. The second is the uplift computed by the series (32), which is shown by the blue crosses. We see that there is an excellent match between the analytical solution (32) and the finite element solution. The third curve is green and shows the simple 1D based uplift estimate. The 1D uplift estimate gets better as pressure distribution spreads out.

Figure 10 shows that Fourier coefficients for case 3 (at 10 years) is dominated by the 5 first wavelengths, and that the following Fourier coefficients for increasingly shorter wavelengths are almost zero. Case 1 (at 0.1 year) is characterized by small Fourier coefficients relative to the injection pressure and they are of nearly the same size for the first 11 terms in the series. Figure 10 shows the f-function values for the Fourier coefficient and we see that $f \approx 0$ for $n > 10$. Figure 9b shows the pressure p_u of equation (32). The uplift is directly proportional to this pressure, where the Fourier coefficients are increasingly damped by the f-function with increasing n. The analytical uplift by expression (32) shows that if the f-function had been one for all wavelengths, then the 1D approximation would have been an exact relation. Wide pressure distributions, which is dominated by the longest wave lengths, have the associated f-function values close to 1. Therefore, wide pressure distributions of just a few dominating long wavelengths become only weakly modified by the filter effect of the f-function. The simple 1D estimate works for such cases. We can use condition (30) to decide how wide a distribution must be. The critical wavelength is $\lambda_c = 6283$ m for these three cases with $h_1 = 1000$ m and figure 9 shows that only case 3 has a pressure distribution wider than λ_c.

9. Conclusion

Large scale CO_2 injection leads to build-up of reservoir fluid pressure, which again leads to poroelastic expansion of the reservoir. The expansion can be observed as surface uplift. We present a plane-strain solution for the displacement field produced by a reservoir overpressure, when the overpressure is represented as a Fourier series.

The solution is derived in two steps, when considering a single term in the Fourier series of the overpressure. A first step gives the displacement field and the uplift for the reservoir layer alone. This solution is the basis for the next step, a two-layer model of a pressurized reservoir with an overburden. The vertical displacement at the surface gives the uplift. We show a case study for the Utsira formation in the North Sea, where the uplift can be approximated with a 1D solution. The analytical model for uplift is well suited to study when the 1D estimate is applicable. Answers are given in terms of the wavelengths for the one-layer and two-layer models. For the one-layer model, the 1D estimate is accurate for wavelengths larger than 2π times the thickness of the reservoir layer. For the two-layer model, the 1D estimate is accurate for wavelengths larger than a critical wavelength, which is 2π times the maximum of the reservoir thickness and the overburden thickness. We show three examples of surface uplift computed from Fourier series representing three stages in an expanding overpressure plume. The examples show how the Fourier solution for the uplift approaches the 1D estimate as the plume gets wider. An analysis of the terms in Fourier series tells that only terms with a wavelength longer than the critical wavelength contribute significantly to the surface uplift. The analytical expressions for the reservoir expansion and uplift are tested against finite element simulations and the match is excellent.

10. Appendix A: Solutions for the displacement field for a reservoir layer

The system of linear inhomogeneous differential equations (19)-(20) becomes homogeneous when u is replaced by a displacement v defined as

$$u = \frac{\alpha p_0}{(2+\gamma)Gk}\sin(kx) + v. \tag{33}$$

The equations for the displacement field (v, w) are then

$$\begin{aligned}(2+\gamma)v_{,xx} + v_{,zz} + (1+\gamma)w_{,xz} &= 0 &(34)\\ (1+\gamma)v_{,xz} + w_{,xx} + (2+\gamma)w_{,zz} &= 0 &(35)\end{aligned}$$

A periodic solution of the of equations (34) and (35) is written

$$\begin{aligned}v &= \left(v_1 e^{cz} + v_2 e^{-cz}\right)\sin(kx) &(36)\\ w &= \left(w_1 e^{cz} + w_2 e^{-cz}\right)\cos(kx) &(37)\end{aligned}$$

Notice that the solutions (36) and (37) for v and w, respectively, do not contain the elastic parameter γ. The reason for that is that both v and w are also solutions of the biharmonic, $\nabla^4 v = 0$ and $\nabla^4 w = 0$, which is a parameterless equation, see Fung [12].

Inserting the solutions (36) and (37) into equations (34) and (35) lead to $c = k$, $w_1 = -v_1$ and $w_2 = v_2$. The boundary condition $w = 0$ for $z = 0$ gives that $v_1 = v_2$, which is conveniently represented as $w_0/2$. The solution for v and w is then

$$\begin{aligned}v &= w_0 \cosh(kz)\sin(kx) &(38)\\ w &= -w_0 \sinh(kz)\cos(kx) &(39)\end{aligned}$$

The remaining parameter w_0 is obtained by the boundary condition on the surface (22), where the normal stress is zero, which gives that

$$w_0 = -\frac{\alpha p_0}{(2+\gamma)Gk\cosh(kh)} \tag{40}$$

The parameter w_0 gives the solution (23) and (24).

11. Appendix B: Solutions for the displacement field in the overburden above a reservoir

Appendix A gives that the solution for the displacement field for the reservoir is

$$u_A = c_0\sin(kx) + w_0\cosh(kz)\sin(kx) \tag{41}$$
$$w_A = -w_0\sinh(kz)\cos(kx) \tag{42}$$

when there is zero displacement at the base of the reservoir and where

$$c_0 = \frac{\alpha p_0}{(2+\gamma)Gk}. \tag{43}$$

We also have from Appendix A that the solution for displacement field in a layer with zero fluid pressure, such as the overburden, is

$$u_B = \Big(u_3 e^{cz} + u_4 e^{-cz}\Big)\sin(kx) \tag{44}$$
$$w_B = \Big(-u_3 e^{cz} + u_4 e^{-cz}\Big)\cos(kx) \tag{45}$$

There are now three parameters which have to be obtained from boundary conditions. One boundary condition is the zero normal stress on the surface of the overburden

$$\sigma_{zz}(z{=}z_2) = \Lambda\frac{\partial u}{\partial x} + (\Lambda+2G)\frac{\partial w}{\partial z} = 0 \tag{46}$$

and the two other boundary conditions express that the displacement field is continuous on the interface between the reservoir and the overburden

$$u_A(z{=}z_1) = u_B(z{=}z_1) \tag{47}$$
$$w_A(z{=}z_1) = w_B(z{=}z_1) \tag{48}$$

These two boundary conditions give that

$$u_3 = \frac{1}{2}\Big(c_0 e^{-kz_1} + w_0\Big) \tag{49}$$
$$u_4 = \frac{1}{2}\Big(c_0 e^{kz_1} + w_0\Big) \tag{50}$$

Finally, zero stress on the surface of the overburden gives

$$w_0 = -c_0\frac{\cosh(kz_2 - kz_1)}{\cosh(kz_2)}. \tag{51}$$

When w_0 from (51) is inserted into expressions (49) and (50) for parameters u_3 and u_4, respectively, and in equations (41) and (42), it gives the displacement field in both the reservoir and the overburden. The amplitude of the vertical displacement at the surface ($z = z_2$) becomes

$$\begin{aligned} A_B(z = z_2) &= -u_3 e^{cz_2} + u_4 e^{-cz_2} && (52)\\ &= -\frac{1}{2}\Big(c_0 e^{-kz_1} + w_0\Big)e^{cz_2} + \frac{1}{2}\Big(c_0 e^{kz_1} + w_0\Big)e^{-cz_2} && (53)\\ &= -c_0 \sinh(kz_2 - kz_1) - w_0 \sinh(kh_2) && (54) \end{aligned}$$

Replacing w_0 and c_0 by equations (51) and (43), respectively, gives the expression of the amplitude A_B in equation(28).

12. Acknowledgement

Parts of this work have been supported by the Research Council of Norway through the projects 233736/E20 ‘Protect”, 244570/E30 “StressLess”, Total and Statoil.

References

[1] Amirlatifi, A., Eckert, A., Nygaard, R., Bai, B., 2011. Estimation of reservoir uplift, seismicity and failure likelihood during co2 injection through coupled reservoir simulation. Society of Petroleum Engineers , 1–11.

[2] Andersen, O., Nilsen, H.M., Gasda, S., 2017. Modeling geomechanical impact of fluid storage in poroelastic media using precomputed response functions. Computational Geosciences .

[3] Andersen, O., Nilsen, H.M., Gasda, S.E., 2016. Modelling geomechanical impact of CO2 injection and migration using precomputed response functions, in: ECMOR XV - Proceedings of 15th European Conference on the Mathematics of Oil Recovery, 29 August - 1 September, 2016, European Association of Geoscientists and Engineers, Amsterdam, Netherlands. pp. 1–26.

[4] Bachu, S., 2008. CO2 storage in geological media: role, means, status and barriers to deployment. Progress in Energy and Combustion Science 34, 254–273.

[5] Benson, S., Cole, D, R., 2008. CO2 sequestration in deep sedimentary formations. Elements 4, 325–331.

[6] Bickle, M., 2009. Geological carbon storage. Nature Geoscience 2, 815–819.

[7] Biot, M., 1941. General theory of three dimensional consolidation. Journal of Applied Physics 12, 155–164.

[8] Bissell, R., Vasco, D., Atbi, M., Hamdani, M., Okwelegbe, M., Goldwater, M., 2011. A full field simulation of the In Salah gas production and CO2 storage project using a coupled geo-mechanical and thermal fluid flow simulator. Energy Procedia 4, 3290–3297.

[9] Bjørnarå, T., Mathias, S., Nordbotten, J., Park, J., 2014. Fast evaluation of fluid-rock coupling in CO2 storage, in: Fourth EAGE CO2 Geological Storage Workshop, EAGE, Stavanger, Norway. pp. 1–4.

[10] Bryant, E., 1997. Climate Process and Change. Cambridge University Press, Cambridge, UK.

[11] Fjær, E., Holt, R., Raaen, A., Risnes, R., Horsrud, P., 2008. Petroleum Related Rock Mechanics, 2nd edition. Elsevier.

[12] Fung, Y., 1968. Foundations of Solid Mechanics. Prentice-Hall.

[13] Gasda, S., Wangen, M., Bjørnarå, T., Elenius, M., 20w17. Investigation of caprock integrity due to pressure build-up during high-volume injection into the Utsira Formation. Energy Procedia 114, 3157–3166.

[14] Geertsma, J., 1966. Problems of rock mechanics in petroleum production engineering, in: IDISRM-1CONGRESS-1966-099, International Society for Rock Mechanics and Rock Engineering, Lisbon, Portugal. pp. 1–10.

[15] Geertsma, J., 1973. Land subsidence above compacting oil and gas reservoirs. Journal of Petroleum Technology 59, 734–744.

[16] Helland, E., et al., 2011. CO2 Storage Atlas, Norwegian North Sea, 2, http://www.npd.no/Global/Norsk/3-Publikasjoner/Rapporter/PDF/CO2-ATLAS-lav.pdf.

[17] International Energy Agency, 2016. Energy snapshot, Global energy-related carbon dioxide emissions 1980 - 2016, https://www.iea.org/newsroom/energysnapshots.

[18] Kim, J., Selvadurai, A., 2015. Ground heave due to line injection sources. Geomechanics for Energy and the Environment 2, 1–14.

[19] Kim, J., Tchelepi, H.A., Juanes, R., 2011a. Stability, accuracy and efficiency of sequential methods. Society of Petroleum Engineers SPE 119084, 1–20.

[20] Kim, J., Tchelepi, H.A., Juanes, R., 2011b. Stability and convergence of sequential methods for coupled flow and geomechanics: Fixed-stress and fixed-strain splits. Computer Methods in Applied Mechanics and Engineering 200, 1591–1606.

[21] Kreyszig, E., 2011. Advanced engineering mathematics. John Wiley & Sons.

[22] Langtangen, H.P., 2003. Computational Partial Differential Equations: Numerical Methods and Diffpack Programming. Springer-Verlag New York, Inc., Secaucus, NJ, USA. 2 edition.

[23] Li, C., Laloui, L., 2016. Coupled multiphase thermo-hydro-mechanical analysis of supercritical CO2 injection: Benchmark for the In Salah surface uplift problem. International Journal of Greenhouse Gas Control 51, 394–408.

[24] Li, C., Paul Barès, P., Laloui, L., 2015. A hydromechanical approach to assess CO2 injection-induced surface uplift and caprock deflection. Geomechanics for Energy and the Environment 4, 51–60.

[25] Merxhani, A., 2016. An introduction to linear poroelasticity. arXiv:1607.04274.

[26] Niu, Z., Li, Q., Wei, X., 2017. Estimation of the surface uplift due to fluid injection into a reservoir with a clayey interbed. Computers and Geotechnics 87, 198–211.

[27] Onuma, T., Ohkawa, S., 2009. Detection of surface deformation related with CO2 injection by DInSAR at In Salah, Algeria. Energy Procedia 1(1), 21772184.

[28] Preisig, M., Prévost, J.H., 2011. Coupled multi-phase thermo-poromechanical effects. Case study: CO2 injection at In Salah, Algeria. International Journal of Greenhouse Gas Control 5, 1055–1064.

[29] Rinaldi, A.P., Rutqvist, J., 2013. Modeling of deep fracture zone opening and transient ground surface uplift at KB-502 CO2 injection well, In Salah, Algeria. International Journal of Greenhouse Gas Control 12, 155–167.

[30] Rinaldi, A.P., Rutqvist, J., Finsterle, S., Liu, H.H., 2017. Inverse modeling of ground surface uplift and pressure with iTOUGH-PEST and TOUGH-FLAC: The case of CO2 injection at In Salah, Algeria. Computers & Geosciences 108, 98–109.

[31] Rucci, A., Vasco, D.W., Novali, F., 2013. Monitoring the geologic storage of carbon dioxide using multicomponent SAR interferometry. Geophysical Journal International 193, 197–208.

[32] Rutqvist, J., 2011. Status of the tough-flac simulator and recent applications related to coupled fluid flow and crustal deformations. Computers & Geosciences 37, 739–750.

[33] Rutqvist, J., 2012. The geomechanics of CO2 storage in deep sedimentary formations. Geotechnical and Geological Engineering 30, 525–551.

[34] Rutqvist, J., Vasco, D., Myer, L., 2009. Coupled reservoir-geomechanical analysis of CO2 injection at In Salah, Algeria. Energy Procedia 1, 1847–1854.

[35] Rutqvist, J., Vasco, D., Myer, L., 2010. Coupled reservoir-geomechanical analysis of CO2 injection and ground deformations at In Salah, Algeria. International Journal of Greenhouse Gas Control 4, 225–230.

[36] Selvadurai, A., 2009. Heave of a surficial rock layer due to pressures generated by injected fluids. Geophysical Research Letters 36, L14302.

[37] Selvadurai, A., Kim, J., 2016. Poromechanical behaviour of a surficial geological barrier during fluid injection into an underlying poroelastic storage formation, in: Proceedings of the Royal Society A, The Royal Society Publishing. pp. 1–22.

[38] Shi, J.Q., Sinayuc, C., Durucan, S., Korre, A., 2012. Assessment of carbon dioxide plume behaviour within the storage reservoir and the lower caprock around the KB-502 injection well at In Salah. International Journal of Greenhouse Gas Control 7, 115–126.

[39] Vasco, D.W., Ferretti, A., Novali, F., 2008. Reservoir monitoring and characterization using satellite geodetic data: Interferometric synthetic aperture radar observations from the Krechba field, Algeria. Geophysics 73, WA113–WA122.

[40] Verdon, J., Kendall, J., White, D., Angus, D., 2011. Linking microseismic event observations with geomechanical models to minimize the risks of storing CO2 in geological formations. Earth and Planetary Science Letters 305, 143–152.

[41] Vilarrasa, V., Rinaldi, A.P., Rutqvist, J., 2017. Long-term thermal effects on injectivity evolution during CO2 storage. International Journal of Greenhouse Gas Control 64, 314–322.

[42] Vilarrasa, V., Rutqvist, J., Rinaldi, A.P., 2015. Thermal and capillary effects on the caprock mechanical stability at In Salah, Algeria. Greenhouse Gases-Science and Technology 5, 449–461.

[43] Wang, H., 2000. Theory of linear poroelasticity. Princeton University Press.

[44] Wangen, M., Gasda, S., Bjørnarå, T., 2016. Geomechanical consequences of large-scale fluid storage in the Utsira Formation in the North Sea. Energy Procedia 97, 486–493.

[45] Weinberger, H., 1995. A First Course in Partial Differential Equations with Complex Variables and Transform Methods. Blaisdell book in pure and applied mathematics, Dover Publications.

[46] White, J.A., Chiaramonte, L., Ezzedine, S., Foxall, W., Hao, Y., Ramirez, A., McNab, W., 2014. Geomechanical behavior of the reservoir and caprock system at the in salah co2 storage project. Proceedings of the National Academy of Sciences 111, 8747–8752.

[47] Zhou, R., Huang, L., Rutledge, J., 2010. Microseismic event location for monitoring CO2 injection using double-difference tomography. The Leading Edge 29, 201–214.